J. Fluid Mech. (2010), *vol.* 646, *pp.* 471–480. © Cambridge University Press 2010
doi:10.1017/S002211200999351X

Nonlinear dynamics of the elliptic instability

NATHANAËL SCHAEFFER[1,2]† AND STÉPHANE LE DIZÈS[1]

[1]IRPHE, CNRS, University Aix-Marseille, 49 rue F. Joliot Curie, 13013 Marseille, France

[2]LGIT, CNRS, University Joseph Fourier, BP 53, 38041 Grenoble Cedex 9, France

(Received 27 August 2009; revised 16 November 2009; accepted 17 November 2009)

In this paper, we analyse by numerical simulations the nonlinear dynamics of the elliptic instability in the configurations of a single strained vortex and a system of two counter-rotating vortices. We show that although a weakly nonlinear regime associated with a limit cycle is possible, the nonlinear evolution far from the instability threshold is, in general, much more catastrophic for the vortex. In both configurations, we put forward some evidence of a universal nonlinear transition involving shear layer formation and vortex loop ejection, leading to a strong alteration and attenuation of the vortex, and a rapid growth of the vortex core size.

1. Introduction

Vortices are ubiquitous in fluid flows and are observed at all scales, from the smallest scales of turbulence to the largest astrophysical scales. Although they are robust structures, they exhibit rich dynamical behaviours which are not all well understood. The two-dimensional dynamics of vortices have been largely studied, and numerous intrinsic instabilities of two-dimensional vortices such as the shear instability or the centrifugal instability had been described several decades ago (see e.g. Drazin & Reid 1981). Later, it was discovered that a three-dimensional instability could be due to the interaction of vortices with each other (Moore & Saffman 1975). It was found that this (elliptic) instability was actually due to the strain field induced by the other vortices (see Kerswell 2002 for a review). It is now believed that this instability could affect the dynamics of the trailing vortex pair generated by aircraft (Laporte & Corjon 2000). For this configuration, the characteristics of the instability in the linear regime obtained in the numerical simulations by Laporte & Leweke (2002) and in low-Reynolds-number experiments by Leweke & Williamson (1998) have been found to be in good agreement with the theory of Le Dizès & Laporte (2002).

Weakly nonlinear theories exist for a single vortex in a strain field (Sipp 2000) and for the rotating flow in a cylinder (Waleffe 1989; Eloy, Le Gal & Le Dizès 2003; Racz & Scott 2008). In an inviscid framework, these theories predict that the nonlinearity should detune the phase of the instability mode and make its amplitude go back to zero. In a cylinder, viscosity changes this picture as the fixed point, limit cycle, chaos or unbounded growth have been shown to become possible dynamical behaviours (Racz & Scott 2008). Kerswell (1999) and Mason & Kerswell (1999) have also demonstrated that when a fixed point state exists, it is very sensitive to secondary

---

† Email address for correspondence: Nathanael.Schaeffer@obs.ujf-grenoble.fr

instabilities. For a vortex in a strain field or for vortex pairs, no such predictions are available.

Motivated by aeronautical applications, numerical simulations of the dynamics of co-rotating or counter-rotating vortex pairs have been performed by several groups (Laporte & Corjon 2000; Marshall, Brancher & Giovannini 2001; Bristol *et al.* 2004). Complicated nonlinear behaviours, involving vortex loops ejections and partial reconnections, have been observed leading to a more or less rapid destruction of the vortices depending on the configurations. However, no clear picture of the nonlinear evolution of the elliptic instability has been put forward. In this paper, our goal is to fill the gap between these fully nonlinear simulations and the weakly nonlinear theory. By considering simple configurations, our objective is to identify some generic or universal features associated with the nonlinear evolution of the elliptic instability.

2. Framework

In this paper, we consider Lamb–Oseen vortices (i.e. vortices in an open domain) defined by their vorticity field written in cylindrical coordinates as

$$\omega = \Gamma/(\pi a^2)\exp(-r^2/a^2),$$

where Γ and a are the circulation and the radius of the vortex, respectively. This vorticity profile is a self-similar solution of the Navier–Stokes equations, provided that the radius a evolves in a fluid of kinematic viscosity ν according to $a(t)=\sqrt{a_0^2+4\nu t}$. Throughout the paper, time scales are normalized by the vortex initial turnover time $2\pi a_0^2/\Gamma$, and k_z denotes an axial wavenumber.

Two situations are studied: (i) a single vortex in an imposed external strain field and (ii) two parallel counter-rotating vortices straining each other. Our objectives are to understand the nonlinear regime of the elliptic instability in the first idealized configuration for which linear and weakly nonlinear theories have been developed and then to extend the results to a vortex configuration directly useful for practical applications. For both cases, the nonlinear development of the instability is simulated with the three-dimensional pseudo-spectral Cartesian code which has already been used and tested by Roy *et al.* (2008). This code uses the three-dimensional fast Fourier transform of the FFTW library (Frigo & Johnson 2005), and aliasing is avoided by using the standard 2/3 rule. The spatial resolution is typically $256 \times 256 \times 48$ in the (x, y, z) directions where $0z$ is the vortex axis, but some simulations have been performed at $512 \times 512 \times 64$.

The base flow of case (i) is computed using a two-dimensional Navier–Stokes code in cylindrical geometry (finite difference scheme in radial direction and Fourier decomposition in azimuthal direction). This code allows us to impose a fixed strain field for large radial coordinates (fixed here at $R = 15\,a_0$). Starting from an initial condition composed of the axisymmetric Lamb–Oseen vortex plus a uniform strain field of strain rate ε, the flow is found to relax on a non-viscous time scale to the quasi-steady strained vortex solution obtained by Jiménez, Moffatt & Vasco (1996). The accuracy of this solution is then checked by comparing the numerical strain rate at the vortex centre with the theoretical prediction (Jiménez *et al.* 1996; Eloy & Le Dizès 1999). This two-dimensional solution evolves slightly owing to viscous diffusion. This effect is known to influence the development of the elliptic instability (Eloy & Le Dizès 1999). For case (i), we have chosen to freeze artificially the base flow in order to identify more clearly the nonlinear effects on the instability and to be able to compare our results with the weakly nonlinear theory. This choice is also

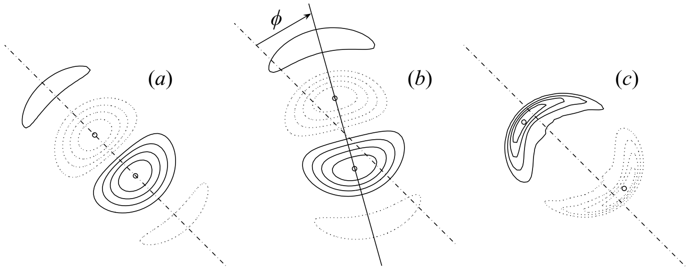

FIGURE 1. Contour plot of the vorticity perturbation of the most unstable mode ($k_z = 2.25$). (*a*) In the linear regime; (*b*) at $t = 960$ for $\varepsilon = 0.005$, $Re = 6300$; (*c*) at $t = 200$ for $\varepsilon = 0.01$, $Re = 10\,000$. Cases (*b*) and (*c*) correspond to the angle and the amplitude circled in figure 2. Solid and dashed lines are positive and negative isovorticity contours, respectively. The two circles indicate the maximum and minimum of each mode from which the angle ϕ is computed.

motivated by applications of the results to the larger Reynolds number flows for which viscous diffusion is negligible. Nevertheless, this assumption will be relaxed for the two counter-rotating vortices case. It will allow us to check that it does not significantly influence the nonlinear dynamics of the instability.

3. Vortex in a strain field

For this case, two sets of parameters are considered: $\varepsilon = 0.005$, $Re = \Gamma/\nu = 6300$ and $\varepsilon = 0.01$, $Re = 10\,000$. The nonlinear development of the elliptic instability is computed by simulating the Navier–Stokes equations for the perturbations u, using the three-dimensional pseudo-spectral code. The size of the box along the vortex axis is set to a single wavelength of the most unstable linear mode. Without nonlinear terms, we let the flow perturbation corresponding to this mode emerge from white noise until the growth rate converges. We then start the nonlinear simulation with a perturbation scaled to a small amplitude such that the linear growth of the instability is always observed before nonlinear effects become significant.

3.1. *Weakly nonlinear regime*

For $\varepsilon = 0.005$, the onset of the elliptic instability is at $Re = 5416$. The first computation at $Re = 6300$ is performed close to the stability threshold in order to look at a weakly nonlinear regime. The dimensionless linear growth rate at this Reynolds number is $\sigma = 1.9 \times 10^{-3}$. The evolution of the shape of the most unstable mode, $k_z = 2.25$, is displayed in figure 1(*a*,*b*). While the linear eigenmode is perfectly aligned with the stretching axis (figure 1*a*), the nonlinear effects cause a slight rotation of the structure, as predicted by the weakly nonlinear theory of Sipp (2000). The mode structure is almost unmodified during this simulation. The dynamics of the angle ϕ as defined in figure 1(*b*) can be analysed as the amplitude of the mode increases and are plotted in figure 2. We observe a limit cycle with a small frequency approximately equal to 8.6×10^{-3}. This behaviour was predicted by Racz & Scott (2008) for the weakly nonlinear evolution of a similar instability in a cylinder, but it has been observed for the first time in the case of the elliptic instability of a strained vortex. Note that in the inviscid framework, no limit cycle is expected in the weakly nonlinear regime: the angle should rotate towards the direction of the compression of the strain field and the amplitude should return to zero (Sipp 2000). The time evolution of the mean axial vorticity profile (z- and θ-averaged) is shown in figure 3. The slow periodic oscillation associated with the limit cycle can be seen on this plot. Note also that the

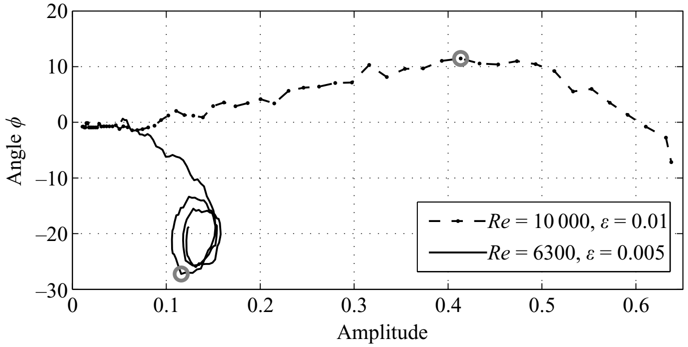

FIGURE 2. Evolution of the angle (in degrees) and amplitude of the instability mode in the two cases. Solid line: $\varepsilon = 0.005$, $Re = 6300$. Dashed line: $\varepsilon = 0.01$, $Re = 10\,000$. The axial vorticity structure of the instability mode at the circles is shown in figure 1.

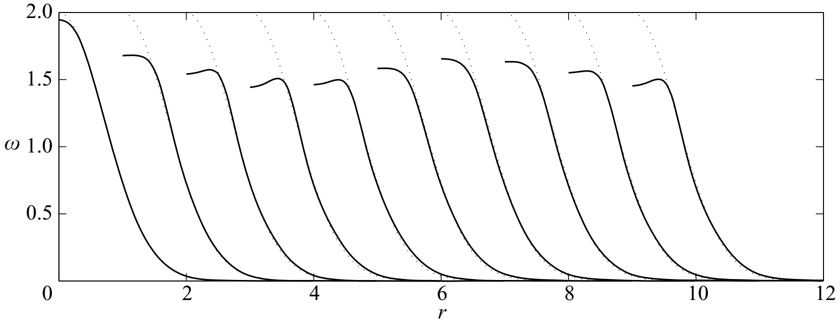

FIGURE 3. Mean vorticity profiles (z- and θ-averaged) as a function of the radial coordinate (scaled with the initial vortex radius) at different instants for the Lamb–Oseen vortex in a small strain field for $\varepsilon = 0.005$, $Re = 6300$. Profiles are separated by $\Delta t = 200$ (scaled with the turnover time) and shifted by $\Delta r = 1$ (exception: between profiles 4 and 6, $\Delta t = 100$). The first profile on the left is at $t = 0$ and the unperturbed profile is repeated in dotted style for reference.

perturbation affects only the vortex core, by draining the mean vorticity out of the centre, while almost no effects are visible outside the core, contrary to what we will now observe for the second set of parameters.

3.2. *Highly nonlinear regime*

In the second simulation of case (i), we are much above the threshold. The linear growth rate is now $\sigma = 1.08 \times 10^{-2}$, that is about six times higher than in the previous case. The evolution of the energy of the different modes is plotted in figure 4. The unstable mode is growing as predicted by the linear theory of Le Dizès & Laporte (2002), and there is no visible departure from the linear growth until $t \simeq 120$, but the mode structure is not observed to rotate as in the previous case. The orientation angle slightly increases instead of decreasing as the amplitude grows (see figure 2). This behaviour was demonstrated as a possible weakly nonlinear regime by Racz & Scott (2008), but here it may also be due to the fact that we are far from the threshold. Indeed, the mode structure is rapidly strongly modified (figure 1*c*) such that the weakly nonlinear theory hypothesis is no longer satisfied. The evolution becomes strongly nonlinear as illustrated in figure 5, suggesting that there is no saturation mechanism. In these snapshots, we clearly observe the formation of secondary vortex

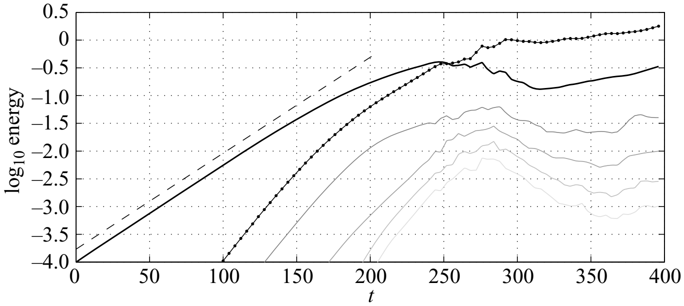

FIGURE 4. Energy of the fundamental mode and its harmonics as a function of time, showing the linear growth and saturation of the elliptic instability. The energy of the fundamental mode $k_z = k_{z0} = 2.25$ and its successive harmonics $k_z = 2k_{z0}, 3k_{z0}, 4k_{z0}, 5k_{z0}$ are given by the plain black line and the grey-scale lines, respectively; the dotted line represents the energy of the mean flow correction ($k_z = 0$) and the dashed line gives the slope of the linear growth. Case (i) for $\varepsilon = 0.01$, $Re = 10\,000$.

structures around the main vortex. These structures, which resemble vortex loops, move away from the vortex axis and become unstable. Small scales are then created, but they are quickly damped by viscosity. After this disordered regime, the main vortex reforms; but because some vorticity has moved away from the initial vortex core, it is now much larger and has a weaker vorticity peak. This evolution can also be seen in figure 6, which displays the mean vorticity profile as a function of time. Note that the formation of a thin layer on the mean vorticity profile is clearly visible on the fifth profile at $t = 240$. The trace of the expelled vortex structures observed in figures 5(c, d) can also be associated with the secondary peak seen in the sixth profile. These features are also visible in supplementary movie 1 (available at journals.cambridge.org/flm) showing the three-dimensional evolution of an isosurface of the total vorticity.

3.3. *A universal mechanism for vortex core growth*

In the strongly nonlinear simulations we observe that the size of the vortex core, defined as the second moment of the vorticity distribution, increases during the process. Moreover, after the breakdown of the vortex and the relaminarization of the flow, an elliptic instability can grow again, widening the vortex a step further.

Figure 7 shows the evolution of the vortex core size for $\varepsilon = 0.005$ at two different Reynolds numbers. For each case, the following features are observed:

(i) The core radius increases during the growth of the elliptic instability;

(ii) It stops when small scales are generated and the vortex has been sufficiently altered;

(iii) The vortex relaminarizes while keeping its radius constant; and

(iv) Eventually, a new elliptic instability develops leading to another growth of the core radius.

What is not apparent in figure 7 is that even though the second-order moment (vortex core size) remains constant, the flow is very time-dependent and resembles the last two rows of figure 5 at the beginning and at the end of the plateau, respectively.

The two different Reynolds number flows exhibit the same qualitative behaviour, but the larger Reynolds number leads to a larger increase in the radius for a given step. This is in agreement with the saturation of the elliptic instability through viscous effects. It also takes longer (time is normalized by multiplying by the growth rate,

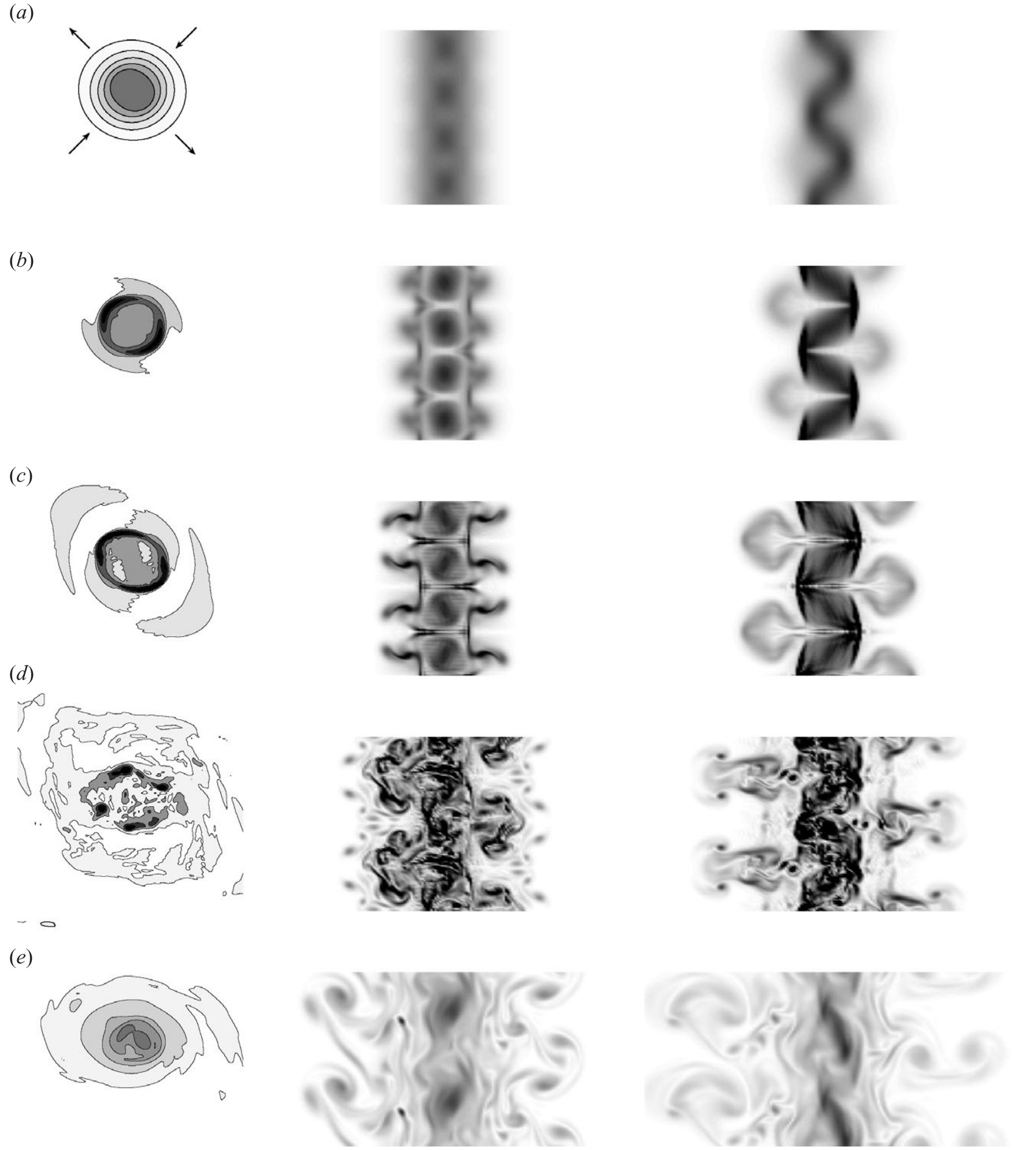

FIGURE 5. Axially averaged vorticity contours in a plane perpendicular to the vortex axis (left) and total vorticity maps in longitudinal planes containing the vortex axis oriented along the direction of compression (middle) and of stretching (right) at different times (from top to bottom: $t = 120$, 200, 240, 280, 360). In the left snapshots, the spatial scale is the same for all snapshots, so is the grey scale which maps zero vorticity to white and $\omega = 2$ to black. The contours are equidistant vorticity levels ranging from minimum to maximum vorticity of each snapshot. For every longitudinal cut, the grey scale (white for $\omega = 0$ to black for $\omega > 3$) and the spatial scale are the same.

which is close to the inviscid one in both cases) for the vorticity field to recover from the breakdown (relaminarization plateau) and before the process can start over again.

In these simulations, only the most unstable wavenumber and its harmonics have been considered. We suspect that the recovery time before the next elliptical instability growth could be shorter if the other wavenumbers were present.

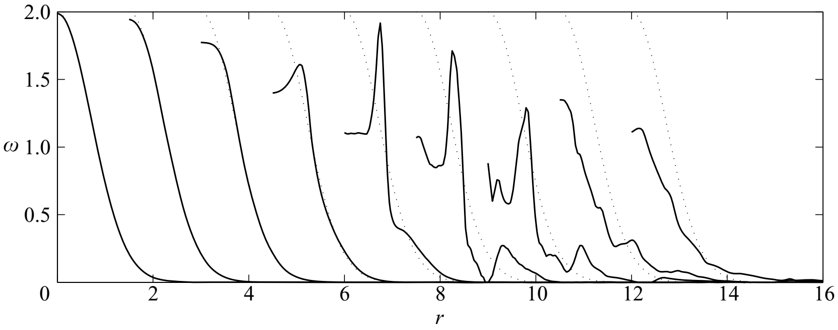

FIGURE 6. Same as in figure 3 but for $\varepsilon = 0.01$ and $Re = 10\,000$. Profiles are here separated by $\Delta t = 40$ (scaled with the turnover time) and shifted by $\Delta r = 1.5$. The first profile on the left is at $t = 80$.

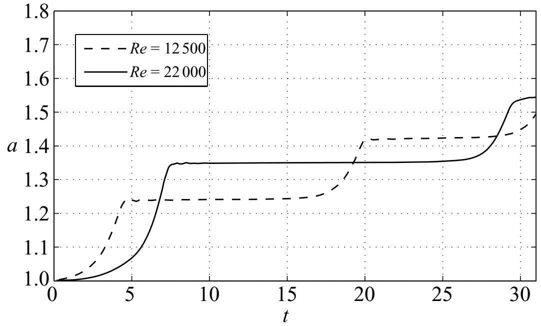

FIGURE 7. Evolution of the vortex radius as a function of time, under the nonlinear effect of several growth of an elliptic instability, for two different Reynolds numbers and the same strain rate $\varepsilon = 0.005$. For each curve, time is normalized by multiplying by the growth rate of the elliptic instability.

The above simulations allow us to put forward the following points:

(i) The main effect of nonlinear evolution of the elliptic instability is to increase the effective vortex core size;

(ii) The process can happen more than once; and

(iii) A small elliptic deformation can lead to a large increase in the core size.

All the observations suggest that the widening of the vortex core through elliptic instability may be very generic and at work in all vortex systems at high Reynolds numbers.

4. Counter-rotating vortices

The simulations of the two counter-rotating vortices system have been performed to check the robustness of the nonlinear scenario observed for case (i). In that case, the strain field responsible for the elliptic instability in each vortex is generated by the other vortex. As both vortices have to adapt themselves to the strain generated by their neighbour, we first perform a two-dimensional simulation to obtain the basic flow, with the same three-dimensional pseudo-spectral code. This two-dimensional simulation was initialized by a field composed of two Lamb–Oseen vortices of opposite circulation $\pm\Gamma$, same radius a_0 and separated by a distance b such that $b/a_0 = 5.5$.

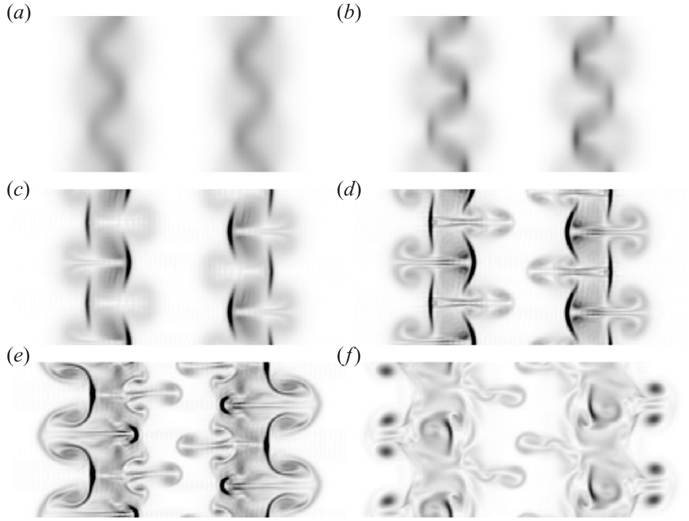

FIGURE 8. Elliptic instability in vortex pairs. Total vorticity maps in the plane containing both vortex axes at different times (*a–f* : $t = 22$, $t = 42$, $t = 62$, $t = 78$, $t = 88$, $t = 100$). The grey scale goes from white ($\omega = 0$) to black ($\omega > 5$) and is the same in each snapshot.

The vortex cores grow slowly by diffusion, but are also elliptically deformed by the strain and quickly reach a quasi-stationary state as in case (i) (see Sipp, Jacquin & Cossu 2000; Le Dizès & Verga 2002 for details). We then stop the simulation when $b/a(t) = 5$, which will be our basic state with Reynolds number $Re = 6300$.

For these parameters, the equivalent external strain rate is $\varepsilon = (a/b)^2 = 0.04$ and the linear growth rate is $\sigma = 4.2 \times 10^{-2}$, so that we are far above the instability threshold and the strongly nonlinear evolution as in case (i) is expected. Counter-rotating vortex pairs are also known to be unstable to a long-wavelength (Crow) instability. This instability is responsible for the formation of vortex rings (Leweke & Williamson 1998), and is expected to grow simultaneously with the short-wavelength elliptic instability we are interested in. Here, the Crow instability is filtered out by considering periodic boxes of small axial length. No interactions between both instabilities are therefore taken into account. The nonlinear development of the Crow instability has been considered elsewhere (Marshall *et al.* 2001; Bristol *et al.* 2004).

Contrary to case (i), the base flow is now allowed to diffuse by viscosity during the nonlinear evolution of the perturbations. The three-dimensional simulations are however initialized by the most unstable linear eigenmode of the base flow obtained at the end of the two-dimensional simulation with a small amplitude (1 %). The time evolution of the total vorticity in the plane containing the vortex axes is shown in figure 8. As for case (i), movie 2 (see *J. Fluid Mech.* website) shows the three-dimensional evolution of vorticity. We can see that the nonlinear dynamics are qualitatively similar to what has been plotted in figure 5. Thin layers of vorticity are formed at the periphery of the vortex, and vortex loops are ejected from the vortex core (compare for example figure 5*c* with figure 8*c, d*). These secondary vorticity structures are then destabilized and dissipated by viscosity. The new vortices which form after this nonlinear evolution are, as for the single vortex case, larger and weaker (figure 9). The average profiles of the last snapshot ($t = 100$) are shown in figure 9 for each vortex. The vortex circulation is conserved, but the radius computed from the second-order moment of the distribution gives $a = 1.68$, whereas a purely

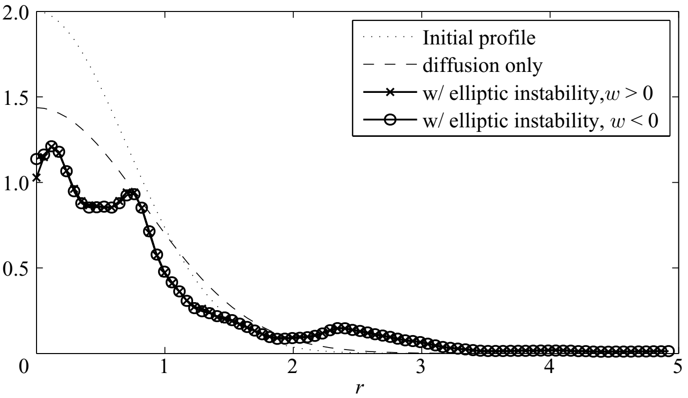

FIGURE 9. Mean vorticity profiles (z- and θ-averaged) as a function of the radial coordinate (scaled with the initial core radius) after 100 turnover times, obtained by diffusion only or with the action of elliptic instability, in the case of counter-rotating vortices. The profiles of the two vortices are almost the same.

diffusive evolution would give $a_{diff} = 1.18$ at this Reynolds number. Alternatively, it would require 460 turnover times instead of 100 in order to obtain the same radius by diffusion only.

Other sets of parameters far above the threshold have been considered for both the strained vortex and the two vortex configurations. They have all provided similar evolutions demonstrating the universality of the nonlinear dynamics of the elliptic instability. Experiments for the two-vortex system have been performed by Leweke & Williamson (1998) (see also Laporte & Leweke 2002). Unfortunately, they have not performed vorticity measurement in the late nonlinear regime. However, their dye visualizations (see figure 19 of Leweke & Williamson 1998) exhibit mushroom-like structures which resemble the expelled vorticity structure observed in figure 8(*d*,*e*).

5. Conclusion

In this paper, we have demonstrated that both the weakly nonlinear and the strongly nonlinear evolutions of the elliptic instability were possible. The weakly nonlinear dynamics which have been observed very close to the threshold are characterized by a limit cycle behaviour. The strongly nonlinear dynamics, which have been obtained in most simulations, are much more violent but possess some universal characteristic features. We have shown that the dynamics always follow the following steps:

(i) concentration of the vorticity in thin layers at the periphery of the vortex,

(ii) expulsion of the vortex loops,

(iii) breakdown of the whole structure, and

(iv) relaminarization process leading to the reformation of a weaker and larger vortex.

This process may start again after relaminarization. We claim that this evolution is universal in high-Reynolds-number flows.

The main consequence of these results is that a moderate strain field can lead to a dramatic reorganization of the vortex, in a highly dissipative process, and a rapid modification of its characteristics. In particular, we have seen that the core radius of a strained vortex can increase quickly and significantly by the repeated action of the elliptic instability even if the Reynolds number is large. We suspect that this core growth mechanism is active in the dynamics of trailing vortices generated by aircraft. It could explain the rapid vortex merging of the co-rotating flap and tip vortices, and the turbulent character of their core structure observed before merging (Devenport, Vogel & Zsoldos 1999).

Financial supports from the European Community (FAR-Wake project AST4-CT-2005-012238) and from the French National Agency for Research (Vortex project ANR-05-BLAN-0241) are acknowledged.

Supplementary movies available at journals.cambridge.org/flm.

REFERENCES

BRISTOL, R. L., ORTEGA, J. M., MARCUS, P. S. & SAVAŞ, Ö. 2004 On cooperative instabilities of parallel vortex pairs. *J. Fluid Mech.* **517**, 331–358.

DEVENPORT, W. J., VOGEL, C. M. & ZSOLDOS, J. S. 1999 Flow structure produced by the interaction and merger of a pair of co-rotating wing-tip vortices. *J. Fluid Mech.* **394**, 357–377.

DRAZIN, P. G. & REID, W. H. 1981 *Hydrodynamic Stability*. Cambridge University Press.

ELOY, C. & LE DIZÈS, S. 1999 Three-dimensional instability of Burgers and Lamb–Oseen vortices in a strain field. *J. Fluid Mech.* **378**, 145–166.

ELOY, C., LE GAL, P. & LE DIZÈS, S. 2003 Elliptic and triangular instabilities in rotating cylinders. *J. Fluid Mech.* **476**, 357–388.

FRIGO, M. & JOHNSON, S. G. 2005 The design and implementation of FFTW3. *Proc. IEEE* **93** (2), 216–231.

JIMÉNEZ, J., MOFFATT, H. K. & VASCO, C. 1996 The structure of the vortices in freely decaying two-dimensional turbulence. *J. Fluid Mech.* **313**, 209–222.

KERSWELL, R. R. 1999 Secondary instabilities in rapidly rotating fluids: inertial wave breakdown. *J. Fluid Mech.* **382**, 283–306.

KERSWELL, R. R. 2002 Elliptical instability. *Annu. Rev. Fluid Mech.* **34**, 83–113.

LAPORTE, F. & CORJON, A. 2000 Direct numerical simulations of the elliptic instability of a vortex pair. *Phys. Fluids* **12** (5), 1016–1031.

LAPORTE, F. & LEWEKE, T. 2002 Elliptic instability of trailing vortices: experiment and direct numerical simulation. *AIAA J.* **40** (12), 2483–2494.

LE DIZÈS, S. & LAPORTE, F. 2002 Theoretical predictions for the elliptic instability in a two-vortex flow. *J. Fluid Mech.* **471**, 169–201.

LE DIZÈS, S. & VERGA, A. 2002 Viscous interaction of two co-rotating vortices before merging. *J. Fluid Mech.* **467**, 389–410.

LEWEKE, T. & WILLIAMSON, C. H. K. 1998 Cooperative elliptic instability of a vortex pair. *J. Fluid Mech.* **360**, 85–119.

MARSHALL, J. S., BRANCHER, P. & GIOVANNINI, A. 2001 Interaction of unequal anti-parallel vortex tubes. *J. Fluid Mech.* **446**, 229–252.

MASON, D. M. & KERSWELL, R. R. 1999 Nonlinear evolution of the elliptical instability: an example of inertial wave breakdown. *J. Fluid Mech.* **396**, 73–108.

MOORE, D. W. & SAFFMAN, P. G. 1975 The instability of a straight vortex filament in a strain field. *Proc. R. Soc. Lond.* A. **346**, 413–425.

RACZ, J.-P. & SCOTT, J. F. 2008 Parametric instability in a rotating cylinder of gas subject to sinusoidal axial compression. Part 2. Weakly nonlinear theory. *J. Fluid Mech.* **595**, 291–321.

ROY, C., SCHAEFFER, N., LE DIZÈS, S. & THOMPSON, M. 2008 Stability of a pair of co-rotating vortices with axial flow. *Phys. Fluids* **20**, 094101.

SIPP, D. 2000 Weakly nonlinear saturation of short-wave instabilities in a strained Lamb–Oseen vortex. *Phys. Fluids* **12** (7), 1715–1729.

SIPP, D., JACQUIN, L. & COSSU, C. 2000 Self-adaptation and viscous selection in concentrated two-dimensional dipoles. *Phys. Fluids* **12** (2), 245–248.

WALEFFE, F. 1989 The 3D instability of a strained vortex and its relation to turbulence. PhD thesis, Massachusetts Institute of Technology.